Journal of Magnetic Resonance 204 (2010) 273–280

Contents lists available at ScienceDirect

Journal of Magnetic Resonance

journal homepage: www.elsevier.com/locate/jmr

Improved *k–t BLAST* for fast fMR imaging ☆

Neelam Sinha [a,*], Manojkumar Saranathan [b], A.G. Ramakrishnan [a]

[a] *Department of Electrical Engineering, Indian Institute of Science, Bangalore 560012, India*
[b] *Lucas Center, Dept. of Radiology, Stanford University CA, USA*

ARTICLE INFO

Article history:
Received 14 August 2009
Revised 3 March 2010
Available online 15 March 2010

Keywords:
fMRI imaging
Under-sampling
Unaliasing
k–t BLAST

ABSTRACT

A popular dynamic imaging technique, *k–t BLAST* (*ktB*) is studied here for fMR imaging. *ktB* utilizes correlations in *k*-space and time, to reconstruct the image time series with only a fraction of the data. The algorithm works by unwrapping the aliased Fourier conjugate space of *k–t* (*y–f*-space). The unwrapping process utilizes the estimate of the true *y–f*-space, by acquiring densely sampled low *k*-space data. The drawbacks of this method include separate training scan, blurred training estimates and aliased phase maps.

The proposed changes are incorporation of phase information from the training map and using generalized-series-extrapolated training map. The proposed technique is compared with *ktB* on real fMRI data. The proposed changes allow for *ktB* to operate at an acceleration factor of 6. Performance is evaluated by comparing activation maps obtained using reconstructed images. An improvement of up to 10 dB is observed in the PSNR of activation maps. Besides, a 10% reduction in RMSE is obtained over the entire time series of fMRI images. Peak improvement of the proposed method over *ktB* is 35%, averaged over five data sets.

1. Introduction

Images with high spatial and temporal resolution are essential in medical diagnosis in applications like dynamic contrast-enhanced MRI or functional MRI (fMRI), where dynamic events are monitored. Today, fMRI has the potential to probe neurophysiological activation in the brain at a much higher spatial resolution than that offered by other non-invasive neuroimaging techniques like PET. The high sensitivity measurement of "Blood Oxygenation Level Dependent" (BOLD) signal modulation points to regions in the cortex responsible for the underlying activity. Currently fMRI applications interrogate neural activity changes only on the order of seconds, although neural activity happens on time scales of the order of milliseconds.

Methods that accelerate imaging speed typically suffer from loss in SNR. But given the fact that the dynamic physiological changes are successfully captured, they find application in imaging non co-operative, pediatric and senior patients. They are also used in breath-held scans where the already sick patient cannot be expected to remain still and hold his/her breath for long. In applications such as diffusion-weighted imaging which typically requires scans of the order of minutes, such accelerated methods would be very useful. In order to facilitate dynamic imaging, one needs to determine the adequate temporal and spatial sampling rates, which has been extensively researched in [2–4]. Enhancement changes that occur in tumors due to contrast uptake, are continuous and aperiodic functions, while dynamic events such as cardiac activity and typical brain-study experiments are periodic or quasi-periodic functions. The periodicity of the dynamic events leads to discreteness in temporal frequency.

In the work reported in [5], the authors represented the continuously changing object in a multi-dimensional, k_x–k_y–*t*-space, as a function of spatial frequencies and a temporal variable. The Fourier conjugate of this multi-dimensional space corresponds to *x–y–f*-space, which is equivalent to the former in terms of energy, based on Parseval's theorem. The sparse energy distribution in *x–y–f*-space, was explored to determine sampling schemes that could effectively trade-off between spatial and temporal samples. The work reported in [6] utilizes a generalized harmonic model for dynamic imaging of objects with periodic or quasi-periodic time variations. The approach converts the problem to one of parameter identification. "UNaliasing by Fourier-encoding the Overlaps using the temporal Dimension" (UNFOLD) was proposed by [7] in order to speed-up acquisition exploiting the periodicity of the underlying event. The method hinges on transfer of information from the *k*-axes to the *t*-axis, making it sufficient to acquire a smaller but denser *k–t*-space. UNFOLD involves a reduction of the dynamic FOV. This FOV reduction diminishes the amount of spatial information acquired along the *k*-axes of *k–t*-space. Because of aliasing,

☆ An earlier brief version of this paper has appeared in [1].

* Corresponding author. Fax: +91 80 23600444.
E-mail addresses: neel.iam@gmail.com (N. Sinha), manojsar@stanford.edu (M. Saranathan), ramkiag@ee.iisc.ernet.in (A.G. Ramakrishnan).

1090-7807/$ - see front matter © 2010 Elsevier Inc. All rights reserved.
doi:10.1016/j.jmr.2010.03.007

spatially distinct points within the object are overlapped at the same spatial position in the images. UNFOLD uses time to label the overlapped components, such that a Fourier transform through time can resolve them. The authors present results on cardiac and fMR imaging, illustrating significant reductions in the acquisition time. More recently in [8], a method for dynamic imaging was proposed and is called *k–t BLAST*. Both UNFOLD and *k–t BLAST* exploit the sparseness in *y–f*-space for accelerated imaging, but differ in their approach towards unaliasing. Unaliasing in UNFOLD involves designing of separate filters about each of the peaks along temporal frequency. However, in *k–t BLAST* the approximate distribution of signal in *y-f*-space should be known in order to unalias, and hence additional training data needs to be acquired. In this paper, we study *k–t BLAST* method and propose enhancements for improved performance.

2. *k–t BLAST*

In [8], *k–t BLAST* (*ktB*) was proposed for reconstruction of dynamic images using regularly undersampled data acquisitions. The correlations in both *k*-space and time are exploited for estimating the unacquired data. A missing data point is estimated based on other available points, within its vicinity in both *k*-space and time. The advantage of this approach is that it exploits more of the relevant correlations, thus improving the estimation of missing data. This improvement could be used to obtain better reconstructed images or achieve higher reduction in data acquisition leading to better temporal resolution. Several variations of *ktB* have been proposed to customize the image reconstruction algorithm for applications such as angiography and cardiac imaging [9–11].

Dynamic MRI can be seen as acquisition of a changing *k*-space signal at different time instants, which is essentially sampling in a higher dimensional *k–t*-space. Here, *k* stands for multi-dimensional *k*-space. Since we are dealing with 2D *k*-space, and it is known that all points along the read-out (k_x) dimension are available, we need to undersample only along phase-encode dimension (k_y). Hence, the mention of *k*-axis would refer to the actual k_y-axis, whose Fourier conjugate axis would be the spatial dimension *y*. For the explanation that follows, please refer Fig. 1. The lattice along which these points are acquired in *k–t*-space is referred to as the *k–t* sampling pattern. The conjugate space obtained upon Fourier transformation of the *k–t*-space is the *y–f*-space. It is observed that the signal distribution in *y–f*-space is very sparse, especially for fMRI with its temporal periodicity of activated pixels. This feature can be used to pack *y–f*-space densely, allowing higher acceleration factors. Under-sampling in *k–t*-space leads to an aliased signal distribution in *y–f*-space.

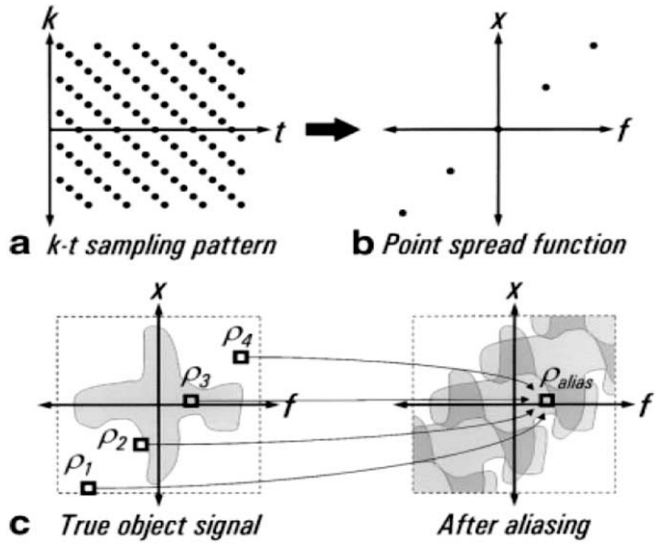

Fig. 1. Knowing sampling pattern helps unaliasing the *y-f* space (*Source*: [8]).

For instance, at a given location (y_0, f_0) in the aliased *y–f*-space obtained from the sparsely acquired data, the signal value $\rho_{\text{alias}}(y_0, f_0)$ is actually the sum of the values at $(y_1, f_1) \dots (y_n, f_n)$ on the true *y–f*-space signal distribution. The locations $(y_1, f_1) \dots (y_n, f_n)$ are determined by the *k–t* sampling pattern.

$$\rho_{\text{alias}}(y_0, f_0) = \rho_1(y_1, f_1) + \cdots + \rho_n(y_n, f_n) \tag{1}$$

where *n* is the acceleration factor.

Unaliasing the aliased *y–f* signal distribution is possible because the aliasing pattern is completely known, once the sampling pattern is fixed. The set of under-determined system of equations given by Eq. (1) needs to be solved for every set of aliased voxels. Since infinite solutions exist, the most sensible way would be to minimize a well-designed cost function. Here, weighted-minimum norm solution is preferred. This solution makes use of prior information, wherein a low frequency, alias-free signal distribution is obtained by acquiring the low *k*-space frequencies, forming the "training map". The values of the training map form the initial estimates in order to obtain the solution given by,

$$\rho = \mathbf{M}^2 \cdot \mathbf{1}^H (\mathbf{1} \cdot \mathbf{M}^2 \cdot \mathbf{1}^H)^{-1} \cdot \rho_{\text{alias}} \tag{2}$$

where $\mathbf{M}^2 = diag(|m_1|^2, \dots, |m_n|^2)$, and $|m_i|$ is the magnitude of the training *y–f* map at the *i*th aliasing location. Here, **1** is the row vector of all **1**s, at *n* positions. Note that the acquisition of the training map data slightly reduces the speed-up effected by the under-sampling pattern. However, the DC-value is separately taken care of, since it is the most important component. The temporal average of the sparse acquisitions forms the DC-value of the estimated *y–f* map.

The new set of equations to be solved is given by,

$$\rho = \underline{\rho} + \mathbf{M}^2 \cdot \mathbf{1}^H (\mathbf{1} \cdot \mathbf{M}^2 \cdot \mathbf{1}^H + \psi)^{-1} \cdot (\rho_{\text{alias}} - \mathbf{1}\underline{\rho}) \tag{3}$$

where $\underline{\rho}$ is the baseline estimate (DC-component) and ψ is the noise variance.

It should be noted that the paradigm frequency decides the harmonics at which the temporal frequency is populated and in turn, the available sparseness in the *y–f*-space. The appearance of the PSF peaks depends on the acceleration factor used. Hence the achievable acceleration factor is governed by the paradigm frequency. An acceptable acceleration factor would be one, where each of the aliased PSF peaks appears such that the overlap between the PSFs occurs where the signal levels are very low.

3. Improvements proposed

Two novel changes have been proposed for improving the performance of *ktB*. They are:

- Improved training map using generalised series extrapolation.
- Phase constraints from the training data.

The emphasis is on obtaining the unaliased map by integrating the magnitude component from the *k–t BLAST* algorithm and the phase component from the training data, as shown in Fig. 2. Several works [9–11] that have explored the utility of *k–t BLAST* for angiography and cardiac imaging have also proposed variations to the sampling scheme. For instance, in [10], the authors have proposed dense sampling in an elliptic region around the center of the *k*-space, while in [11], the authors use sliding window reconstruction of the undersampled data. Here we utilize the variable-density sampling scheme proposed in [9].

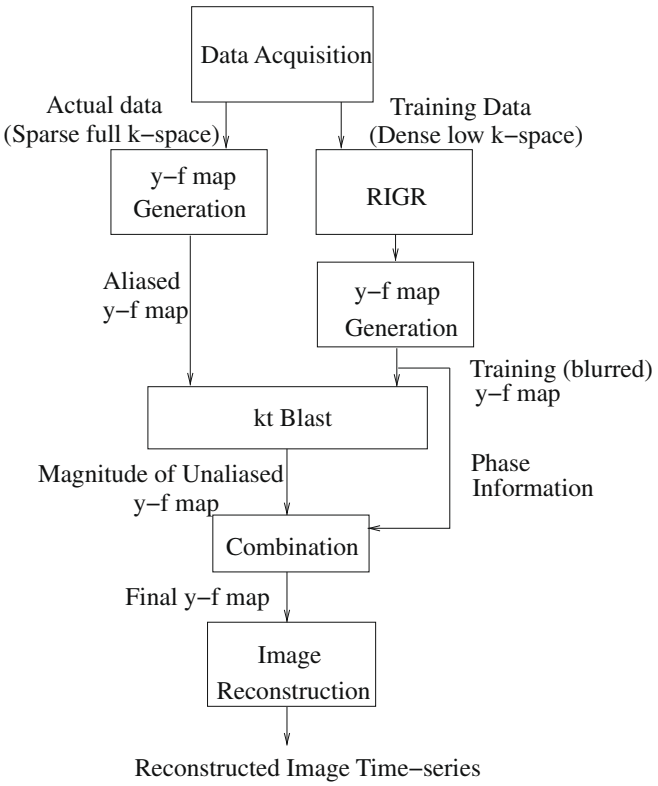

Fig. 2. Overview of the proposed enhancements to *k–t BLAST*.

3.1. Data acquisition

In the original *ktB* scheme [8], the training and actual data are acquired at disjoint instants of time, and follow different sampling schemes. The training data contains only the low *k*-space frequencies, while the actual data acquisition is along a pre-designed sparsely sampled lattice, as shown in Fig. 3a. A variation of data acquisition scheme that couples both the training and actual scans is shown in Fig. 3b. This is a variable-density sampling lattice. This scheme minimizes the mis-registration between the training and data scans. This scheme of acquisition reduces the acceleration factor achievable, but eliminates possible artifacts due to mis-registration. In the experiments reported here, this variable-density sampling scheme has been utilized. A similar data acquisition scheme was reported by Xu et al. [12], where full k_y data was acquired at the first and last time frames, whereas only low k_y for all the time frames in between. However, in the work proposed here, full k_y data is not acquired in the last time frame, thus reducing the data acquisition time. The data acquisition scheme followed in the proposed work is shown in Fig. 3c.

3.2. Training map

Hansen et al. [13] report how the quality of training data influences the working of *ktB*, in contexts where training and actual data are acquired at disjoint instants of time. They report that increasing the number of time frames of acquisition of training data decreases the reconstruction error negligibly. They also report that filtering of the training data in order to reduce truncation artifacts has minor impact on reconstruction errors.

However, in a variable-density acquisition scheme, training data is available at all the time frames of the experiment. We explored the impact of including higher frequencies in the training data, on the working of *ktB*. We compared *ktB* reconstructions that use low *k*-space frequencies in the training data against those that use all the *k*-space frequencies (ideal training data). It is seen that the errors can be brought down by a factor of 2, using higher frequencies in the training map. The disparity in the quality of two image reconstructions led us to explore the possibility of obtaining an improved-resolution training map using the acquired low *k*-space frequencies. It must be observed that at locations in the aliased *y–f*-space, where the signal is dominated by noise, the values from the training map (that are chosen as estimates), can lead to meaningful results only if the estimate is close to the truth.

The proposed method generates an improved-resolution training map, despite acquiring only the lower spatial frequencies. This is achieved by extrapolation using the generalized series model, which requires one full-resolution acquisition. A static image was obtained at the start of the experiment in each of the cases, to serve as the full spatial resolution reference image This high-resolution static acquisition serves to estimate the missing high-frequencies in the training map. The working of the generalized series modeling is outlined below.

3.2.1. Generalized series modeling

In generalized series modeling, the missing high spatial frequencies are split into two components as follows:

$$d_{GS}(k) = d_c(k) + \sum_m c_m d_c(k - m \cdot \Delta k) \tag{4}$$

where d_{GS} is the generalized series estimate, d_c is the Fourier transform of the static image, c_m are the generalized series coefficients and Δk refers to the spatial-frequency resolution. The first part comes from the apriori static information, whereas the second part comes by adaptively adjusting the coefficients so that data consistency is maintained. We implemented a fast version of this algorithm outlined in [14]. After this extrapolation, it follows that the deviation of the training data from the ideal, full *k*-space training data decreases. We expect better training data to translate to better training maps in *y–f*-space.

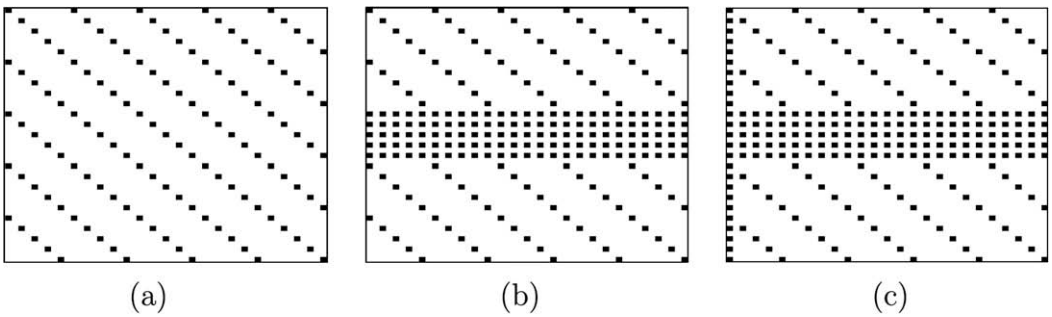

Fig. 3. Data acquisition schemes (*X*-axis – time frame, *Y*-axis – acquired Phase encodes). (a) Uniform density (used in *ktB*). (b) Variable density sampling. (c) Full-resolution static data at the first time frame followed by variable-density sampling scheme (utilized in the proposed work).

In the work reported by Xu et al. [12] also the training data is RIGR-reconstructed before being utilized. The solution proposed by Xu et al. is given as

$$\rho = \rho_{\mathrm{RIGR}} + \mathbf{E}\mathbf{S}^{H}(\mathbf{S}\mathbf{E}\mathbf{S}^{H} + \psi)^{-1}(\mathbf{a} - \mathbf{S}\rho_{\mathrm{RIGR}}) \quad (5)$$

where ρ is a vector of unaliased image spectrum intensities, ρ_{RIGR} is a vector of RIGR image spectrum intensities, **a** is a vector of sensitivity-weighted aliased intensities, **S** is the sensitivity matrix, ψ is the noise correlation matrix, and **E** is the training map. The authors utilize the RIGR-extrapolated data ρ_{RIGR} as the DC-term. The approach proposed by Xu et al. aimed at obtaining a reliable estimate for the DC term of the *y–f* map, rather than use the temporal average as the regularization term as originally proposed in *k–t BLAST* [8]. This approach utilizes generalized series modelling to estimate the DC term. As is well-known, the DC term is most important since it contains maximum energy. The image-adaptive regularization for every time frame leads to improved performance. Hence this approach would be very useful in scenarios where the acquired data is noisy, reducing the occurrence of image artifacts.

However, in the current work, an improved estimate of the training map is obtained using generalized series modelling. This allows higher achievable acceleration factors since the process of unaliasing is given reliable initial values. The approach attempts to obtain unaliased estimates for all frequencies. Hence this approach would be useful in imaging fine structures and phenomena where multiple temporal frequencies are involved, as in brain imaging, where higher frequencies also play an important role.

3.3. Phase constraints

The second change proposed is the incorporation of phase constraints from the training map. The training map, though not of best possible resolution, does contain unaliased signal distributions. In Eq. (3), as given in the original *k–t BLAST* proposition, the phase of the aliased *y–f* map is used, which would be erroneous. Hence, we use the phase information of the training map in estimating the true *y–f* map.

$$\Theta = \angle\rho_{train} \quad (6)$$

$$\tilde{\rho} = |\rho| \exp(i\Theta) \quad (7)$$

where $\tilde{\rho}$ is the final estimate of the signal distribution in *y–f* plane and ρ_{train} is the training map.

Phase maps are typically smooth and are generally estimated using lower frequencies. Hence the unaliased phase of the *y–f* map obtained using low *k*-space acquisitions is in accordance with the procedure used to obtain phase maps. The approach proposed by Xu et al. does not address the issue of aliased phase maps. Aliased phase maps might lead to artifacts restricting the achievable maximum acceleration factor.

4. Experiments and results

4.1. Data utilized for the study

fMRI data is obtained on a 3T scanner for 5 volunteers, for experiments with "visual stimulus". In the course of the experiment, 3 two-dimensional T_2^*-weighted images, each with 64 scans, are acquired using a gradient-echo FLASH sequence (TE/TR 40 ms/80.5 ms, matrix size of 128×64; The image matrices are zero-filled to obtain 128×128 images with a spatial resolution of 1.953×1.953 mm; slice thickness = 5-mm and 2-mm gap). The corresponding two-dimensional anatomical slices are also acquired with a T_1-weighted IR RARE sequence (TI = 900 ms; TE/TR 40 ms/3900 ms, matrix size = 512×512) in the same experimental session. In all the experiments, ON and OFF stimuli are presented with a duration of 5.162 s/sample. Each stimulation period had four successive stimulation ON states followed by four OFF states. The stimulations are repeated for eight cycles (total duration of the experiment is 5.5 mins.). The experiments are carried out at different sessions with different subjects. The visual stimulation task comprised an 8-Hz alternating checkerboard pattern with a central fixation point projected on a LCD system. The subjects are asked to fixate on the point during stimulations. Images are acquired at three axial levels of the brain at the visual cortex.

4.2. Performance evaluation

fMRI images are mainly studied for the activation maps, which interpret the information contained in the entire time series of images. Hence, to evaluate the reconstruction performance, we compare the activation maps obtained against the reference activation map. Statistical Parametric Mapping (SPM2) is the most widely used method for fMRI time series analysis [15]. The primary objective is to detect activated voxels and the resulting statistical parametric maps represent the activation strength of each voxel. The scale of the activation-strength obtained is important, since the activation maps are eventually thresholded to obtain the truly activated regions. Hence, when drastic changes in the scales of activation-strength are observed, the activation maps are considered degraded. Root mean square error (RMSE), correlation with reference, and mean activation level of the activation maps are the performance metrics used to quantify the degradation in activation. If we analyze the true image time series *A* and the reconstructed series *B*, using same SPM method and parameters, we expect comparable scales in activation strength at similar locations in the resulting statistical parametric maps S_A and S_B.

fMRI time series are first realigned to remove movement effects using least-squares minimization [15] and then smoothed using 3D Gaussian kernel with full width at half maximum (FWHM) = 4.47 mm, to decrease spatial noise. Canonical hemodynamic response function (HRF) plus time and dispersion derivatives are used as basis function and changes in BOLD signal associated with the task are assessed on a pixel-by-pixel basis, using the general linear model and the theory of Gaussian fields as implemented in SPM2. This method takes advantage of multivariate regression analysis and corrects for temporal and spatial autocorrelations in the fMRI data. Those voxels in the statistical parametric map are identified as activated, that satisfy $p \leqslant 0.05$, on carrying out an *F*-test.

4.3. Experimental results

MATLAB is used for all simulations. For the trials reported, the training and the actual acquisitions are generated from the full *k*-space, by using appropriate under-sampling masks.

The unaliased training as well as aliased sparse *y–f* maps are shown in Fig. 4a and b, respectively. As claimed earlier, it can be seen that the signal distribution in *y–f*-space is very compact, thus leading to possibilities of achieving higher acceleration factors. In Fig. 5a, the deviation of the training data from the ideal training data is shown for 2 cases. In the first case, the training data is simply zero-padded as in the baseline *ktB*, whereas in the second case, the obtained low *k*-space frequencies are RIGR-extrapolated. Clearly, the RIGR-extrapolated data is seen to be closer to the ideal training data. In Fig. 5b, we compare how the gains of Fig. 5a translate to the *y–f*-space. It can be observed that the RIGR-extrapolated training map is close to the training map that would have been generated had all the frequencies been available for training (ideal training data) and is more accurate than the zero-padded map that the *ktB* algorithm uses.

Fig. 4. Typical *y–f* maps obtained from *k*-space data acquired with an acceleration factor of 5 using: (a) Densely sampled low *k*-space (training data). (b) Undersampled full *k*-space (actual data).

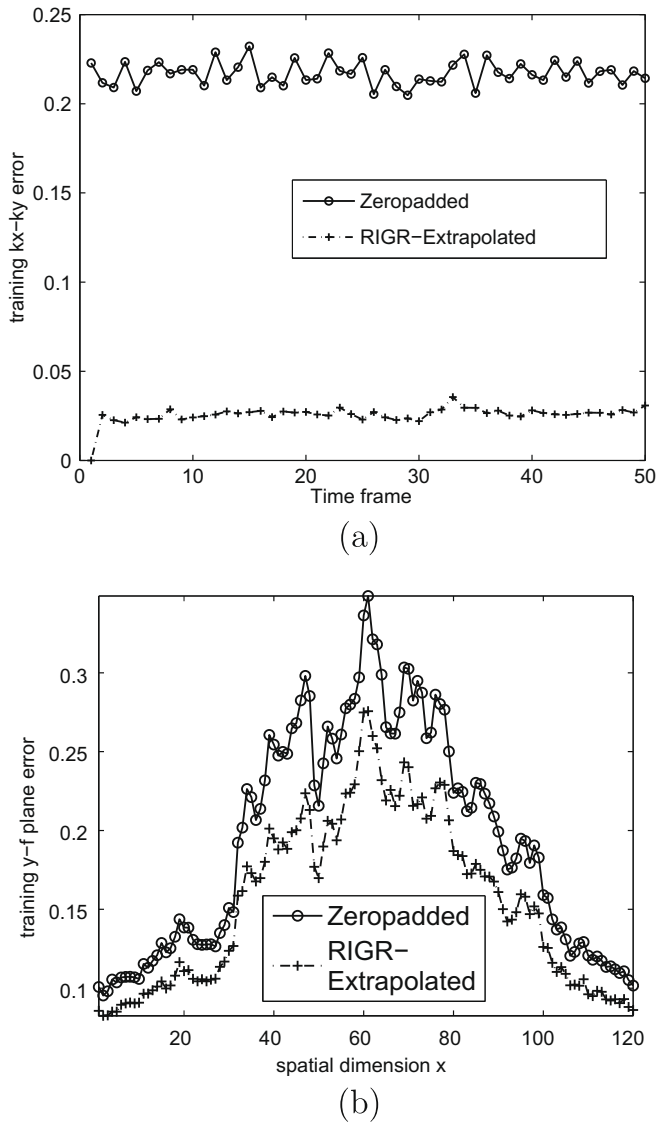

Fig. 5. Performance comparison for acceleration factor of 5: (a) Normalized error in training *k*-space data with respect to the ideal training data. (b) Normalized error in *y–f* training map.

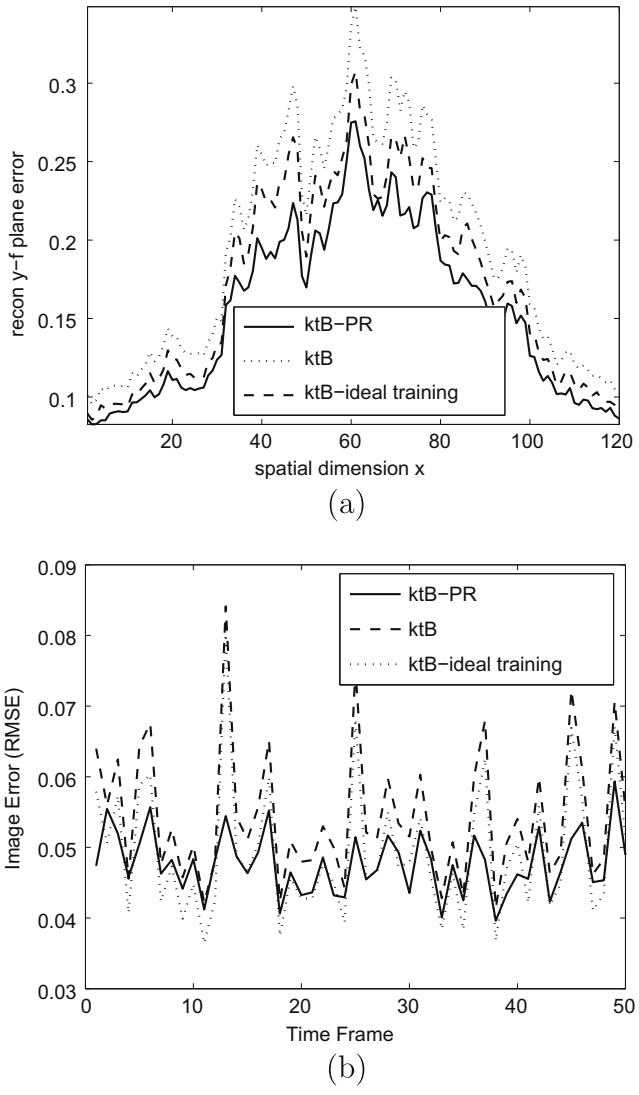

Fig. 6. Normalized reconstruction errors for an acceleration factor of 5: (a) Normalized error in reconstructed *y–f* map. (b) Normalized RMSE of the reconstructed image time series.

In Fig. 6a, we see errors in the reconstructed *y–f* plane as compared to the true *y–f* plane. The three cases compared are: the training map being ideal (*ktB* with ideal training data), zero-padded (*ktB*) and the method proposed here (*ktB*-PR). It can be seen that the proposed case results in lower errors compared to the zero-padded case, consistently for all the instants of the time series. Fig. 6b shows the normalized RMSE of the reconstructed image

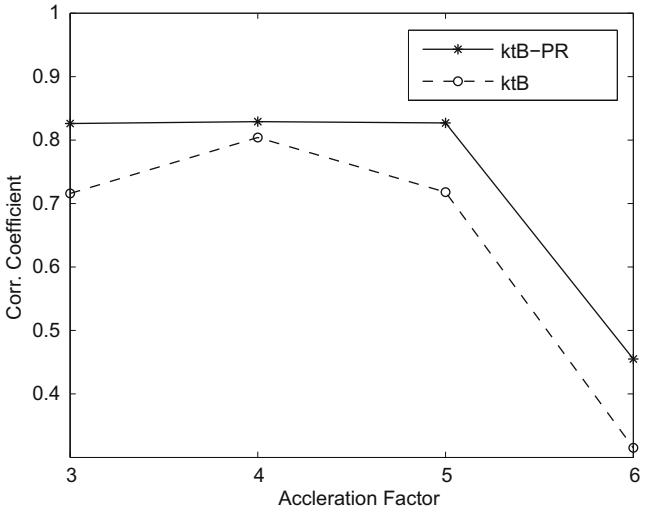

Fig. 7. Correlation of the activation map obtained from the image time series reconstructed using *ktB* and *ktB*-PR with accelerated data acquisition, with the reference activation map obtained using the original image time series.

time series for all the three cases outlined above. It can be seen that the proposed case and the ideal training map case, are comparable, while both consistently outperform the baseline *ktB* reconstruction. It can be observed that the reconstruction with ideal training data is not the best at all time instants. This is because the availability of the entire *k*-space for generation of the training map implies that in Eq. (3), the best estimate for M is obtained. However, the phase of ρ still remains aliased. Hence even though the best estimate for M is available, the final reconstruction suffers due to the aliased phase.

The importance of obtaining unaliased phase is illustrated with a simple example. For an acceleration factor of 2, the resulting aliased signal value c comes from the overlap of unaliased values a and b; thus $c = a + b$. If one of the two contributing unaliased magnitudes is dominant and the other is noise, then unaliasing is efficient. But if the two contributing magnitudes are comparable and phases very dissimilar, then the process of unaliasing suffers.

Fig. 7 shows the decline in the correlation between the obtained activation map and the reference map as a function of the acceleration factor. In Fig. 8, we observe the activation maps obtained using the two methods, for a gain of factor 5 in temporal resolution. Clearly, the map obtained using the proposed method displays less artifacts than the one reconstructed using baseline *ktB*. We also observe that the gain in PSNR goes up to 10 dB. The RMSE of the fMRI time series reduces by about 10% averaged over all the time points, with a peak improvement of 35% compared to the baseline *ktB* for acceleration factors up to 6. For an acceleration factor of 6, we notice that the scales of activation maps obtained using the baseline *ktB* are lower by a factor more than 10, and hence, it is not possible to threshold them to see activated regions. On the other hand, *ktB*-PR results in activation maps that are lower by a factor 2 and hence activated regions can be seen even at lower thresholds. At accelerations above 6, we notice significant degradation in the strength of the activation maps, and hence do not consider them.

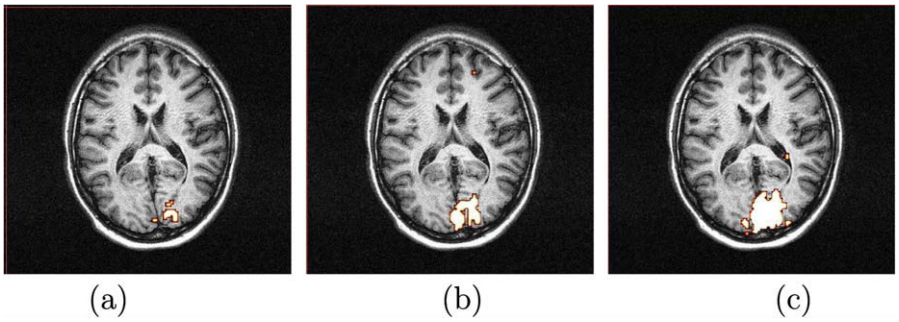

Fig. 8. Thresholded activation maps obtained using SPM for acceleration factor 5, with the image time series reconstructed using: (a) original images, (b) *ktB*-PR, and (c) *ktB*.

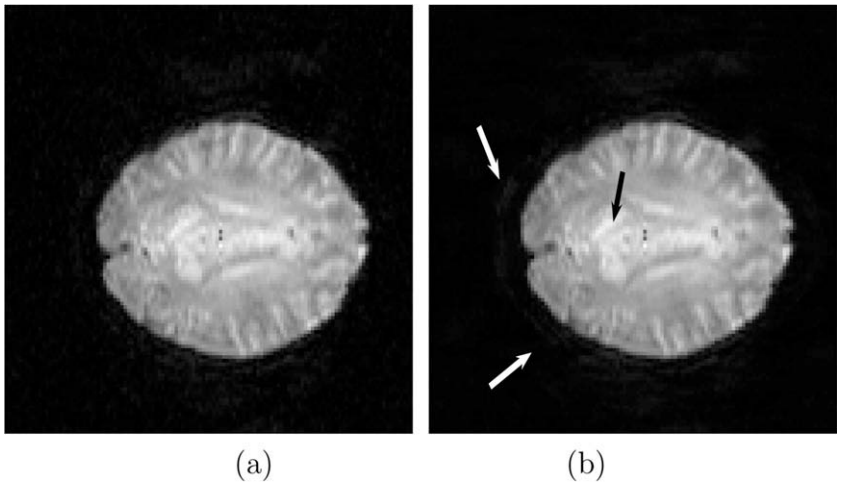

Fig. 9. (a) Sample fMR image from a time series of images. (b) Corresponding *ktB* reconstruction (color scale for all images: 0–255). Arrows indicate regions of significant error.

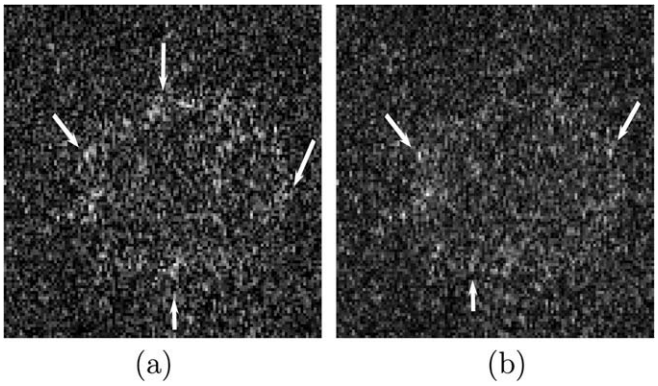

Fig. 10. Comparison of reconstruction performance for the image in Fig. 9. Error image for *ktB* with (a) Regular training data. (b) Ideal training data (color scale for all images: 0–14). Arrows indicate regions of significant error.

5. Discussion

The image shown in Fig. 9a is a sample from the chosen fMR time series. Applying the *ktB* algorithm, we obtain the reconstruction shown in Fig. 9b. Although the two images look perceptibly similar, small intensity differences can be seen on close inspection as in the area pointed to by the arrows. The corresponding error image is shown in Fig. 10a. Now, the same image is reconstructed with a change in the training data set. We assume the ideal case, where all possible training data is available (ideal training data). The error image for the reconstruction obtained in this case is shown in Fig. 10b.

We have also carried out trials where only one of the two proposed changes are made to the existing algorithm. We compare the results (image reconstructions) of each of the following cases:

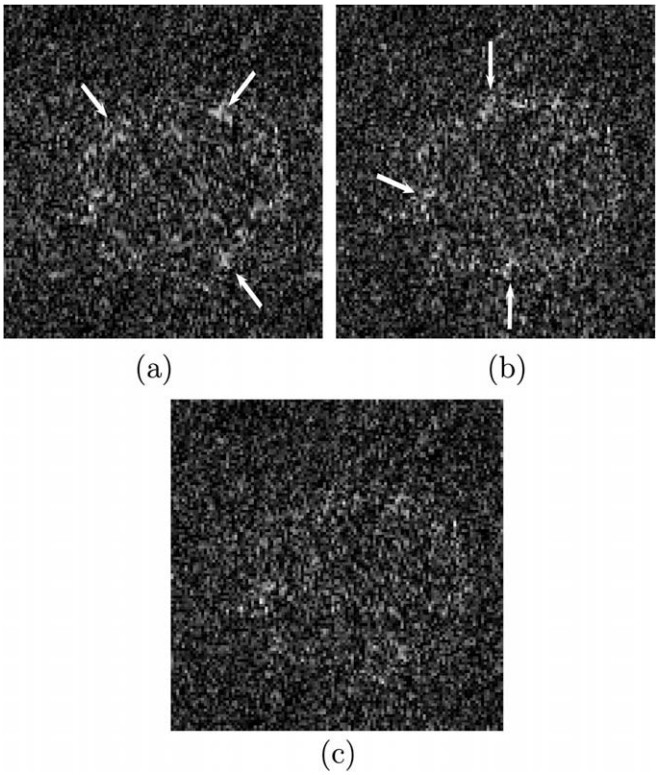

Fig. 11. Reconstruction performance of the proposed improvements on the image shown in Fig. 9a. Error images using *ktB* with: (a) Only phase constraints. (b) Only RIGR-extrapolated training map. (c) Variations utilized in both (a) and (b) (color scale for all images : 0–14). Arrows indicate regions of significant error.

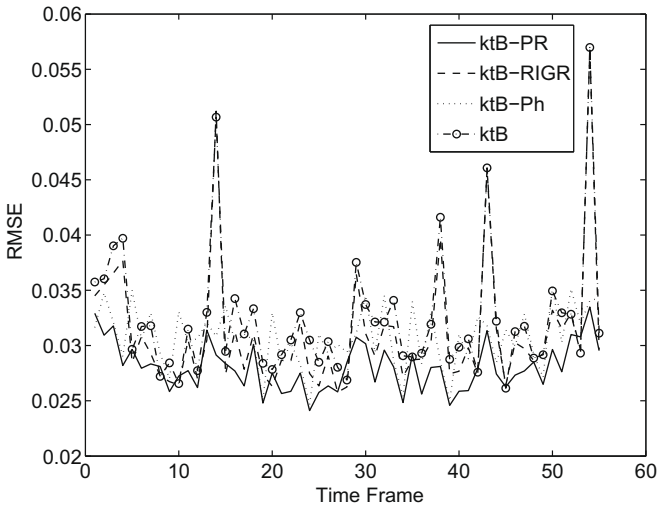

Fig. 12. Performance comparison with each of the proposed variations to *ktB* discussed here. Normalized RMS error is plotted for each of the time series from the error images.

- Only phase constraints are imposed (*ktB*-Ph).
- Only generalized-series-extrapolated training map (*ktB*-RIGR).
- Both the above variations incorporated (*ktB*-PR).

It is observed that incorporating both the changes leads to better reconstruction than that of the baseline *ktB*, as seen from the error images shown in Fig. 11. The plots in Fig.12 show the RMSE obtained for an entire image time series using each of the variations of *ktB* discussed in this paper: *ktB*, *ktB* with phase constraints and no RIGR-extrapolated training map, *ktB* with RIGR-extrapolated training map and no phase constraints and finally *ktB* with both the improvements included. It is observed that *ktB*-PR (*ktB* along with the proposed variations) results in the least RMSE for the image time series reconstruction.

6. Conclusion

In this paper, we have proposed an improved version of the existing dynamic imaging technique *ktB*. A variable-density data acquisition scheme has been utilized, in order to avoid a separate training scan. The generalized-series extrapolated training map is used to serve as an estimate of the true signal distribution in place of the zero-padded training map. Besides, the final solution makes use of the phase constraints from the training map, rather than from the aliased training map. The phase assignment in the original *ktB* is a major source of error. Thus addressing this limitation leads to improved performance. All of the above enhancements are incorporated into the algorithm and applied to real data. Results on fMRI data have shown that these enhancements together lead to improved reconstructions and acceleration factors of up to 6. The reconstruction performance is evaluated using activation maps obtained. We observe an improvement of up to 10 dB in the PSNR of activation maps. The proposed technique results in more accurate activation maps and also the image time series incurs mean RMSE of less than 10% averaged over the entire time series, for acceleration factors of up to 6.

Acknowledgments

We would like to thank Prof. Jagath Rajpakse, NTU, for sharing the fMRI data. Special thanks to his student Ms. Juan Zhou for carrying out the SPM analysis. We thank the anonymous reviewers for helping us to improve the presentation and rigor of the paper.

References

[1] N. Sinha, M. Saranathan, A.G. Ramakrishnan, J. Zhou, J.C. Rajapakse, Ultra-fast fMRI imaging with high-fidelity activation map, in: Proceedings of the International Conference on Neural Information Processing, vol. 2, 2006, pp. 361–368.

[2] W.S. Hoge, An adaptive signal processing approach to dynamic magnetic resonance imaging, Ph.D. thesis, Northeastern University, Boston, 2001.

[3] S. Krishnan, *K*-space acquisition method for dynamic contrast-enhanced MRI: application to breast tumors, Ph.D. thesis, University of Michigan, 2004.

[4] S.K. Shripad, Dynamic contrast-enhanced magnetic resonance imaging, Master's thesis, Department of Electrical Engineering, Indian Institute of Science, Bangalore, India, 2004.

[5] Q.-S. Xiang, R.M. Henkelman, K-space description for MR imaging of dynamic objects, Magn. Reson. Med. 29 (1993) 422–428.

[6] Z.P. Liang, H. Jiang, C.P. Hess, P.C. Lauterbur, Dynamic imaging by model estimation (DIME), Int. J. Imaging Syst. Technol. 8 (1997) 551–557.

[7] B. Madore, G.H. Glover, N.J. Pelc, Unaliasing by Fourier-encoding the overlaps using the temporal dimension (UNFOLD), applied to cardiac imaging and fMRI, Magn. Reson. Med. 42 (1999) 813–828.

[8] J. Tsao, P. Boesiger, K.P. Pruessmann, *k–t* BLAST and *k–t* SENSE: dynamic MRI with high frame rate exploiting spatiotemporal correlations, Magn. Reson. Med. 50 (2003) 1031–1042.

[9] S. Kozerke, J. Tsao, R. Razavi, P. Boesiger, Accelerating cardiac cine 3D imaging using *k–t* BLAST, Magn. Reson. Med. 52 (2004) 19–26.

[10] S. Kozerke, J. Tsao, R. Hoogeveen, J. Puginier, P. Boesiger, K.U. Wentz, Accelerating time-resolved 3D contrast-enhanced angiography using *k–t* BLAST, in: Proceedings of 13th ISMRM, 2005, p. 382.

[11] R. Boubertakh, N.M. Noble, S.R. Hegde, D.L. Hill, R.S. Razavi, Automatic training for *k–t* BLAST reconstruction, in: Proceedings of 13th ISMRM, 2005, p. 2439.

[12] D. Xu, K.F. King, Z.-P. Liang, Improving *k–t* sense by adaptive regularization, Magn. Reson. Med. 57 (2007) 918–930.

[13] M.S. Hansen, S. Kozerke, K.P. Pruessmann, P. Boesiger, E.M. Pedersen, J. Tsao, On the influence of training data quality in *k–t* BLAST reconstruction, Magn. Reson. Med. 52 (2004) 1175–1183.

[14] Z.P. Liang, B. Madore, G.H. Glover, N.J. Pelc, Fast algorithms for GS-model-based image reconstruction in data-sharing Fourier imaging, IEEE Trans. Med. Imaging 22 (8) (2003) 1026–1030.

[15] K.J. Friston, A.P. Holmes, Statistical parametric maps in functional imaging: a general linear approach, Hum. Brain Mapping 2 (1995) 189–210.